Erschienen in: CrystEngComm ; 24 (2022), 44. - S. 7718-7726
https://dx.doi.org/10.1039/D2CE00896C

New insights into the nucleation of magnesium hydroxide and the influence of poly(acrylic acid) during the early stages of $Mg(OH)_2$ crystallisation†

J. Scheck,‡[a] J. K. Berg,‡[a] M. Drechsler,[b] A. Kempter,[c] A. E. S. Van Driessche,[d] H. Cölfen,[a] D. Gebauer*[e] and M. Kellermeier*[f]

Nucleation is a unique process with broad relevance across a wide range of scientific disciplines and applications. While considerable progress in the understanding of the mechanisms underlying the nucleation of minerals from solution has been made for popular model systems such as calcium carbonate, corresponding detailed insights are still missing for other, less prominent minerals. Here, we present a potentiometric titration-based method that allows the early stages of the crystallisation of brucite, $Mg(OH)_2$, to be monitored and quantified. Together with complementary characterisation provided by (cryogenic) transmission electron microscopy, the collected data shed novel light on the species occurring prior to, during, and after nucleation of brucite. In the second part of the work, the newly developed approach was applied to investigate the effects of added poly(acrylic acid) on the different stages of the crystallisation process. The polymer is found to stabilise brucite nanoplatelets and co-precipitate with the inorganic phase, yielding a composite material. The methodology established in this study can readily be used to screen other chemistries for their ability to prevent magnesium hydroxide scaling and/or afford brucite nanomaterials with tailored properties.

Introduction

Over the past ten years, our understanding of the mechanisms underlying the crystallisation of inorganic minerals from aqueous solutions has advanced significantly thanks to a large number of pioneering, and sometimes controversial, studies.[1–5] While many of the key discoveries were made for prominent mineral systems such as calcium carbonate,[6–8] calcium phosphate,[9–11] or iron (oxy)(hydr) oxides,[12–14] other inorganic compounds have received much less attention. In this context, one rather neglected example is magnesium hydroxide. Its mineral form, known as brucite, is moderately abundant in natural settings, where it mainly occurs in ultramafic rocks and forms *via* metamorphosis of magnesium-rich phases like dolomite or periclase.[15] From an industrial point of view, interest in magnesium hydroxide derives from its potential use as flame retardant,[16,17] additive in the processing of paper and pulp,[18] neutralising agent in the treatment of acidic wastewater,[19,20] or for the fabrication of refractory materials.[21] As the constituent ions are omnipresent in seawater, $Mg(OH)_2$ has also been considered as an artificial scaffold for coral colonies.[22] An obvious advantage of magnesium hydroxide in any of its potential applications is the fact that it does not contain CO_2 and hence can be considered a climate-neutral alternative to other minerals like lime or soda. Conversely, brucite has also aroused interest in the context of new technologies for carbon dioxide sequestration.[23,24] However, there are also industrial settings where the formation of magnesium hydroxide is highly undesired, most notably in processes involving aqueous media at high temperatures and/or alkaline pH values. Due to the low solubility of $Mg(OH)_2$ under these conditions, mineralisation may readily occur and lead to incrustation of technical surfaces, which will reduce heat

[a] *Physical Chemistry, University of Konstanz, Universitätsstr. 10, D-78464 Konstanz, Germany*
[b] *Bavarian Polymer Institute (BPI), Keylab "Electron and Optical Microscopy", University of Bayreuth, Universitätsstr. 30, D-95440 Bayreuth, Germany*
[c] *Inorganic Materials & Synthesis, BASF SE, Carl-Bosch-Str. 38, D-67056 Ludwigshafen, Germany*
[d] *Instituto Andaluz de Ciencias de la Tierra (IACT), CSIC – University of Granada, E-18100 Armilla, Granada, Spain*
[e] *Institute of Inorganic Chemistry, Leibniz University Hannover, Callinstr. 9, D-30167 Hannover, Germany. E-mail: gebauer@acc.uni-hannover.de; Fax: +49 (0)511 762 3006; Tel: +49 (0)511 762 18855*
[f] *Material Science, BASF SE, Carl-Bosch-Str. 38, D-67056 Ludwigshafen, Germany. E-mail: matthias.kellermeier@basf.com; Fax: +49 (0)621 66 43388; Tel: +49 (0)621 60 43388*

† Electronic supplementary information (ESI) available: Plot of the ratios of bound ions during titration with and without added polymer (Fig. S1) and results of solution speciation calculations of the concentration of different solutes (Fig. S2) and their activity coefficients (Fig. S3) during the titration experiment.

‡ These authors contributed equally to this work.

transfer and clog pipes.[25–28] Brucite scaling is particularly critical in the desalination of seawater *via* evaporative processes, often in combination with other minerals such as aragonite.

Due to this broad relevance, the crystallisation of magnesium hydroxide from solution has been investigated recurrently in the past. Many of these previous studies determined the rates of $Mg(OH)_2$ nucleation and/or growth as a function of various solution parameters (like supersaturation), or under the influence of different heterogeneous substrates,[25,29–35] often with the aim to identify experimental windows for the formation of uniform brucite particles with controlled morphologies. Other work focused on alterations of existing $Mg(OH)_2$ surfaces, for example in contact with toxic metal cations,[36] during carbonation,[37] or upon transformation to layered double hydroxides.[38] To date, detailed insights into the very early stages of brucite formation from solution and the potential role(s) of crystallisation modifiers in this process are still missing.

In the present work, we have addressed this aspect and investigated $Mg(OH)_2$ nucleation in the absence and presence of poly(acrylic acid) (PAA) as an archetype of polymeric scale inhibitors. Inspired by previous studies of other minerals like calcium carbonate[6,7,39,40] or calcium hydroxide,[41,42] we have developed a potentiometric titration assay, during which magnesium chloride solution is dosed into a reservoir of alkaline water at constant pH (with and without added PAA), while the actual concentration of free Mg^{2+} ions is monitored by an ion-selective electrode (ISE). Progressive hydrolysis of $MgCl_2$ with slowly increasing supersaturation eventually leads to $Mg(OH)_2$ nucleation and growth. During these early stages of crystallisation, samples were drawn at different times and analysed by (cryogenic) transmission electron microscopy (TEM), while the finally formed solid phase was characterised using infrared (IR) spectroscopy and powder X-ray diffraction (PXRD). The results obtained in this way shed novel light on the processes preceding and controlling the nucleation of brucite, and show how polymeric additives interact with the mineral precursors and, thus, allow the course of crystallisation to be modified. The gained insights may help in the design of more efficient $Mg(OH)_2$ antiscalants, as well as in the synthesis of brucite (nano)materials with tailored properties.

Experimental section

Potentiometric titration experiments

In order to induce nucleation of $Mg(OH)_2$, a 20 mM solution of magnesium chloride hexahydrate (Sigma-Aldrich, ≥99.0%) was added continuously at a rate of 0.01 mL min^{-1} to 50 mL water that was previously adjusted to pH 11.0 using 100 mM NaOH solution (Merck, Titripur®). During addition, the pH in the reaction vessel was measured by an immersed electrode (Metrohm, No. 6.0256.100) and kept constant by automatic counter-titration of 100 mM NaOH. Simultaneously, the actual amount of free Mg^{2+} ions was monitored by means of an ion-selective electrode (ISE; C-CIT Sensors AG, model MT050). Read-out of the two sensors and controlled addition was achieved with a titration unit from Metrohm (905 Titrando), to which two dosing units (800 Dosino) for the $MgCl_2$ and NaOH solutions were attached. To study the influence of added poly(acrylic acid) (Sigma-Aldrich, average molecular weight: M_w = 5100 Da, with PDI = $M_w/M_n \approx 2.7$), 10 ppm polymer were dissolved in the initial 50 mL water before starting the titration. All solutions were prepared using water taken from a Millipore® system and purged with nitrogen to remove any dissolved carbon dioxide. During titration, the reaction vessel was flushed with a gentle stream of water-saturated nitrogen to avoid carbonate formation. The pH electrode was calibrated with commercial buffer solutions (Mettler-Toledo, pH values 7.00, 9.21 and 11.00) prior to each experiment. Calibration of the magnesium-selective electrode was carried out by titrating $MgCl_2$ solutions into water at neutral pH under otherwise identical conditions, usually immediately before an actual precipitation assay due to the importance of a proper calibration of the Mg-ISE and its known changes upon ageing. All titration experiments were performed at least in triplicate.

Ex situ characterisation

Precipitates formed at the end of the titration experiments were isolated by centrifugation and subsequent repeated washing with ethanol. After drying in air, the composition of the material was studied by attenuated total reflection infrared spectroscopy (ATR-IR) using a Perkin-Elmer Spectrum 100 instrument, while powder X-ray diffraction (PXRD) patterns were recorded with a Huber G670 Imaging Plate Guinier Camera system using Cu-K_α radiation. For the latter purpose, the isolated precipitates were mounted on a Mylar film with a thickness of 6 μm. For transmission electron microscopy (TEM) and electron diffraction (ED), a drop of the reaction mixture was placed on a carbon-coated copper grid and blotted with a filter paper. After drying, particles present on the grid were investigated on a JEOL JEM-2200FS microscope operated at 200 kV. To gain further insights into the early stages of $Mg(OH)_2$ crystallisation, aliquots were drawn from the reaction vessel at different stages of the titration experiments and investigated by means of cryogenic transmission electron microscopy (cryo-TEM). For this purpose, the liquid samples were applied to lacey carbon-filmed copper grids and blotted using filter paper. The remaining thin film was immediately vitrified by plunging the grids into liquid ethane at its freezing point. The resulting specimens were studied on an EM922 Omega microscope from Zeiss/LEO, equipped with a cooled sample holder that kept the sample at *ca.* 90 K. Collected images were processed with a background-subtraction routine and, optionally, a Butterworth smoothening filter.

Results & discussion

Monitoring the progress of the early stages of precipitation in real time was realised by a titration-based assay, in which $MgCl_2$ solution is added continuously to alkaline water at a constant pH of typically 11.0, giving characteristic profiles for the pre- and early post-nucleation stages as shown in Fig. 1.

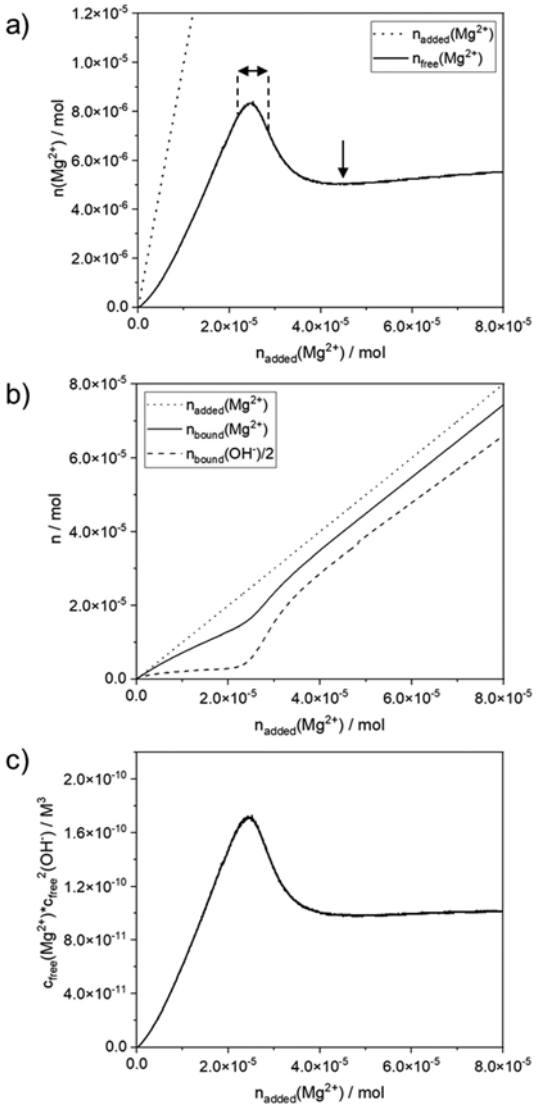

Fig. 1 *In situ* monitoring of the nucleation of magnesium hydroxide by potentiometric titrations of aqueous solutions at a constant pH of 11.0. a) Molar amount of free Mg^{2+} (full line) detected by an ion-selective electrode during addition of 20 mM $MgCl_2$ solution to 50 mL water at a rate of 0.01 mL min^{-1}. The dotted line represents the added amount of $MgCl_2$. Arrows mark the time (or time interval) at which samples were drawn for ambient-temperature and cryogenic transmission electron microscopy (*cf.* Fig. 2). b) Corresponding profiles of bound magnesium ($n_{bound}(Mg^{2+})$, full line) and hydroxide ions ($0.5 \cdot n_{bound}(OH^-)$, dashed line) as compared to the dosed amount of $MgCl_2$ (dotted line) (see Fig. S1 in the ESI† for a plot of the evolution of the $n_{bound}(Mg^{2+})/n_{bound}(OH^-)$ ratio in the course of the titration experiment). c) Free ion product calculated from the measured free concentrations of magnesium and hydroxide ions.

The amount of free magnesium ions in solution ($n_{free}(Mg^{2+})$), tracked by an immersed ion-selective electrode (Fig. 1a), increases as more and more $MgCl_2$ is added up to a point where critical conditions are reached and nucleation occurs. Subsequently, $n_{free}(Mg^{2+})$ decreases as solid particles have formed and continue growing. Prior to the maximum, the detected amount of free magnesium ions is significantly lower (*ca.* 20–25%) than the added quantity ($n_{added}(Mg^{2+})$; dotted line in Fig. 1a), indicating that ion pairs, complexes, and/or larger clusters exist in noticeable fractions in the one-phase system during the pre-nucleation regime – in full analogy to previous observations for other minerals.[6,7,39–42] At $n_{added}(Mg^{2+}) \approx 5$ μmol, the slope of $n_{free}(Mg^{2+})$ becomes steeper, which suggests a change in the stoichiometry of pre-nucleation ion association.

Further insights into the binding behaviour can be gained by evaluating the volume of base needed to keep the pH constant, from which the amount of hydroxide ions bound in associated species ($n_{bound}(OH^-)$) can be derived *via* mass balance considerations and compared to the respective bound amount of magnesium ions ($n_{bound}(Mg^{2+})$). Interestingly, the resulting binding profiles (Fig. 1b) show that the $n_{bound}(Mg^{2+})/n_{bound}(OH^-)$ ratio increases from initially *ca.* 0.3 to levels higher than 1 soon after $MgCl_2$ titration has been started (see Fig. S1 in the ESI†). As nucleation is approached, the excess of magnesium (relative to hydroxide) in bound states becomes more and more pronounced to reach values of around 2.2 at the maximum in $n_{free}(Mg^{2+})$. This means either that the associated species are positively charged on average, and/or that other anions (*e.g.* chloride) participate in complex formation. The latter notion is supported by solution speciation calculations performed using the PHREEQC software package,[43] which predicts the coexistence of $[MgOH]^+$ and $[MgCl]^+$ at all compositions during the pre-nucleation regime (see Fig. S2 in the ESI†). However, $[MgOH]^+$ should be much more abundant (by about two orders of magnitude) and consequently, the data collected in the present work cannot be explained by such mononuclear complexation processes alone. Most likely,

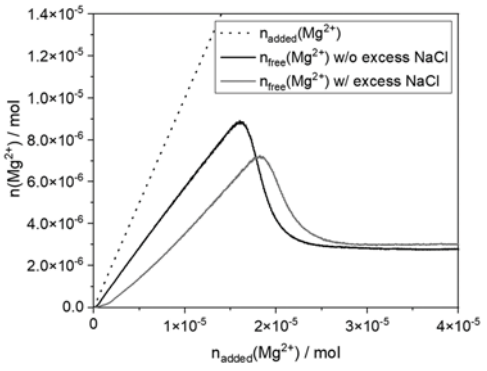

Fig. 2 Development of the amount of free magnesium ions detected upon titration of 20 mM $MgCl_2$ solution into 50 mL of pure water (full black line) and 1 mM NaCl solution (full grey line). The dotted black line represents the amount of dosed $MgCl_2$.

mixed species comprising multiple Mg^{2+} ions as well as OH^- and Cl^- counterions will be formed. Participation of chloride ions in pre-nucleation ion association is further substantiated by titration experiments, in which 1 mM sodium chloride was added to the starting volume. Corresponding data (Fig. 2) show that the slope of $n_{free}(Mg^{2+})$ decreases in the presence of added NaCl, indicating that more magnesium ions are bound at higher chloride concentrations as the equilibrium is shifted towards associated states such as $[MgCl_x]^{(2-x)}$ or $[MgCl_yOH_z]^{(2-y-z)}$. Indeed, the trends observed in Fig. 2 are convoluted to some extent with activity effects caused by the increased ionic strength; however, any such effects should lead to steeper slopes[39] and are likely negligible as the level of $n_{free}(Mg^{2+})$ after nucleation, which is a measure of the solubility product of the formed solid phase, is very similar to that of the reference experiment in pure water.

After nucleation, the profiles of $n_{bound}(Mg^{2+})$ and $0.5{\cdot}n_{bound}(OH^-)$ exhibit very similar slopes and run parallel to the dosed amount, which confirms the formation and growth of $Mg(OH)_2$ after nucleation as expected (Fig. 1b). Offsets of the three profiles along the *y*-axis are likely caused by the assumption of ideal conditions during data evaluation, which is arguably not fulfilled at the given electrolyte concentrations (see Fig. S3 in the ESI† for a plot of changes in the activity coefficients of Mg^{2+} and OH^- during titration, which was calculated using PHREEQC[43] and shows that higher amounts of apparently bound magnesium, as observed in Fig. 1b, are expected for ideal treatment of increasingly non-ideal data). However, the derived ion profiles should still properly reflect the association processes occurring in solution, as demonstrated previously for the calcium carbonate system.[39] Finally, the measured Mg^{2+} and OH^- concentrations can be used to calculate actual free ion products, *i.e.* $c_{free}(Mg^{2+}){\cdot}c_{free}{}^2(OH^-)$. The resulting profiles (Fig. 1c) exhibit classical LaMer-type behaviour and show that the free ion product approaches a constant level after nucleation, from which the apparent solubility of the nucleated phase(s) can be inferred. The measured solubility product (*ca.* 9.9×10^{-11} M^3) is more than one order of magnitude higher than reported values for crystalline brucite (5.6×10^{-12} M^3).[44] These differences may arise from the ideal treatment of the data in the present work, although any correction for non-ideality should actually not affect the resulting solubility products (or, if any, lead to even higher values).[39] Therefore, it is more likely that crystalline brucite coexists with a more soluble phase (*e.g.* amorphous magnesium hydroxide) at this stage, as observed for other minerals.[6]

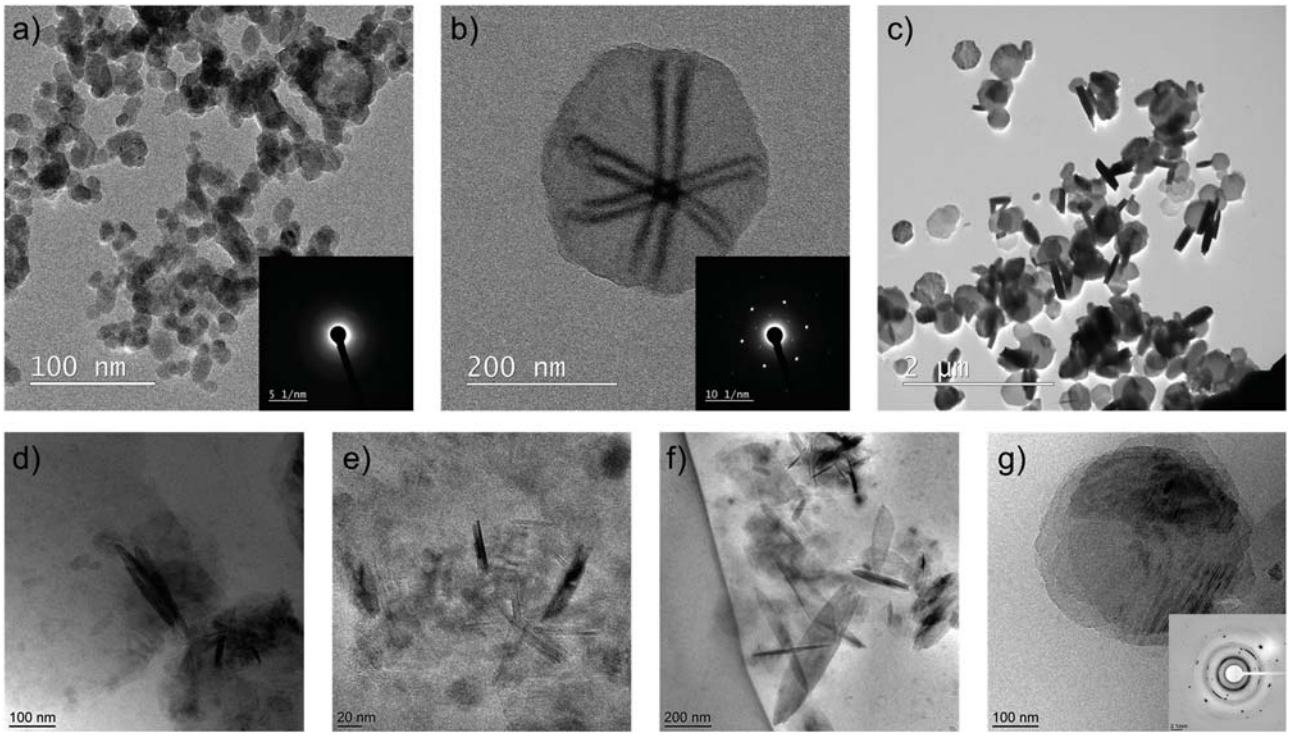

Fig. 3 Characterisation of particles formed during potentiometric titration in the absence of additives by means of transmission electron microscopy in (a–c) dry state at ambient temperature and (d–g) vitrified state under cryogenic conditions. Samples were drawn near the maximum in $n_{free}(Mg^{2+})$ (*cf.* Fig. 1a; sampling interval indicated by dashed lines) (a, b and d–g) or after the subsequent drop to a constant plateau as marked by the arrow in Fig. 1a (c). The inserted electron diffraction patterns identify the particles as being either amorphous (a) or crystalline (b and g), with the observed reflections matching those expected for brucite in the latter case. Note that the cross-like variations in electron contrast observed for the crystal in (b) may arise due to local differences in thickness (for a hexagonal-bipyramidal habit) and/or bending contours caused by tensions in the basal plane.

In order to further elucidate the nature of the species relevant to brucite nucleation, samples were drawn from the reaction vessel around the maximum in $n_{free}(Mg^{2+})$ and characterised using transmission electron microscopy (Fig. 3). In TEM analyses carried out at ambient temperature (Fig. 3a), networks of more or less spherical nanoparticles were repeatedly observed in small amounts across the grid surfaces, with primary particle sizes of 10–20 nm and no distinct crystalline order as indicated by ED patterns. Interestingly, such defined amorphous particles were not present in analogous vitrified samples, where disordered material rather occurred in the form of ill-defined and extended "clouds" without clear-cut boundaries (Fig. 3d and e). This suggests on the one hand that amorphous precursors are involved in $Mg(OH)_2$ nucleation, as for many other mineral systems.[1,2,7–11,40–43] On the other hand, this material is apparently not stable enough to be preserved upon drying and transforms into (arguably less hydrated) nanoparticles. Cryo-TEM images further reveal that crystalline structures start to emerge within the disordered networks (Fig. 3d–f), presumably *via* internal reorganisation processes. Eventually, this yields well-defined hexagonal platelets with diameters ranging from 200 to 400 nm and diffraction patterns consistent with crystalline brucite,[20] as observed independently by both ambient-temperature (Fig. 3b) and cryogenic TEM (Fig. 3g). As more and more $MgCl_2$ is added and the amount of free Mg^{2+} has decreased to a constant level after nucleation, the abundance and maturity of these hexagonal platelets increases and particle aggregation is observed (Fig. 3c).

The developed methodology can be readily applied to investigate the influence of additives on the early stages of brucite crystallisation from solution. Here, we chose poly(acrylic acid) as an archetype of polymeric scale inhibitors for a pilot study. Previous work has shown that polycarboxylates, such as PAA, can have multiple effects during mineral precipitation far beyond the well-known phenomena of ion complexation, threshold inhibition, and bulk particle dispersion.[40–42,45–48] Moreover, polymeric additives bearing carboxylate groups were found to affect the properties of the formed solid precipitates and may thus potentially lead to new (hybrid) materials with interesting morphologies and structures.[49–51]

Typical titration profiles obtained in the presence of 10 ppm PAA (initial concentration) are summarised in Fig. 4 (red curves), in direct comparison to a reference experiment without added polymer (black curves). From the progressions of $n_{free}(Mg^{2+})$ (Fig. 4a) and the $n_{bound}(Mg^{2+})/n_{bound}(OH^-)$ ratio (Fig. 4b), it becomes evident that PAA does not interfere noticeably with ion binding patterns in the pre-nucleation regime, as the respective slopes are almost indistinguishable from those of the reference experiment. The most striking effect of PAA on the crystallisation behaviour is a drastic delay of the maximum in $n_{free}(Mg^{2+})$, *i.e.* nucleation is strongly inhibited. Plots of the free ion product (Fig. 4c) show that about twice the nominal level of

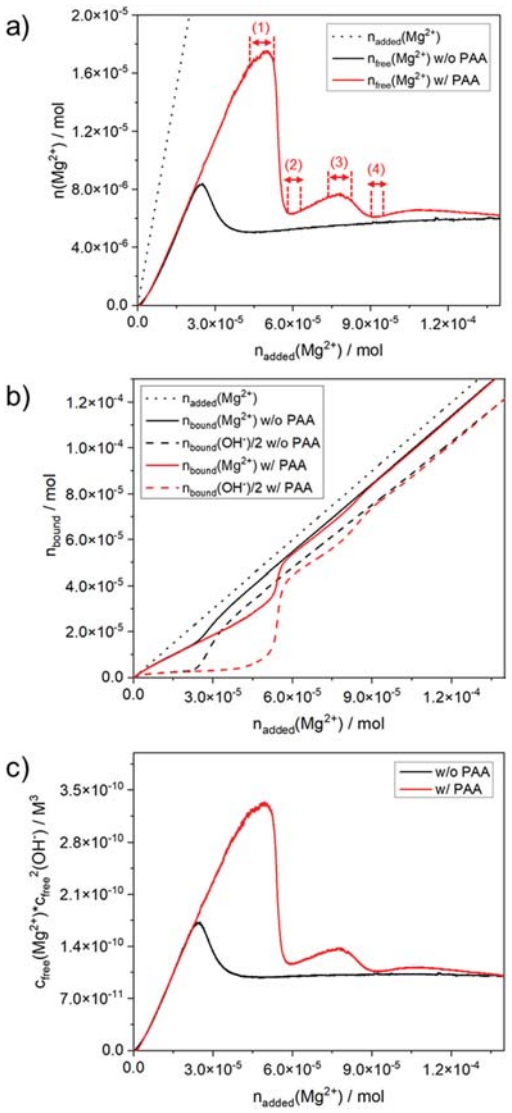

Fig. 4 Results of potentiometric titration assays in the presence of 10 ppm poly(acrylic acid) (red curves) as compared to a reference experiment without any additives (black curves) at a constant pH of 11.0. a) Molar amount of added (dotted line) and detected free (full lines) Mg^{2+} ions. Arrows and dashed lines mark the four time intervals during which samples were drawn for ambient-temperature and cryogenic transmission electron microscopy (*cf.* Fig. 4). b) Corresponding profiles of bound magnesium ($n_{bound}(Mg^{2+})$, full lines) and hydroxide ions ($0.5 \cdot n_{bound}(OH^-)$, dashed lines) as compared to the dosed amount of $MgCl_2$ (dotted line) (see Fig. S1 in the ESI† for a plot of the evolution of the $n_{bound}(Mg^{2+})/n_{bound}(OH^-)$ ratio in the course of the titration experiment). c) Free ion products calculated from the measured free concentrations of magnesium and hydroxide ions.

supersaturation is required for brucite to nucleate under the influence of 10 ppm PAA. During the inhibition period, the ratio of bound ions increases further to reach a threefold excess of Mg^{2+} at the time of nucleation (see Fig. S1 in the ESI†), which suggests that association of chloride (and polyacrylate) ions plays an even more important role than in the absence of the polymer. The formation of $Mg(OH)_2$ after nucleation is again confirmed by a strong increase in

$n_{bound}(OH^-)$ towards the expected 1 : 2 molar ratio (Fig. 4b). This transition in ion binding stoichiometry appears to be slower at the onset of polymer-controlled nucleation, indicating a barrier to dissociation of $[MgCl_x]^{(2-x)}$ and/or $[MgCl_yOH_z]^{(2-y-z)}$ to yield pure hydroxide species. Another key feature induced by added PAA is the fact that the amount of free Mg^{2+} (as well as the free ion product) does not drop to a constant level immediately after nucleation. Instead, a local minimum is observed, subsequent to which $n_{free}(Mg^{2+})$ re-increases and reaches a secondary maximum (*cf.* Fig. 4a). In the following, another such maximum occurs until the amount of free magnesium ultimately approaches the final level measured in the reference experiment. These wave-like post-nucleation patterns signify pronounced growth inhibition, where poisoning by the polymer impedes incorporation of further ions and stabilises the formed particles at small sizes, as also observed for calcium carbonate crystallisation in the presence of PAA.[40,46,47]

After initial nucleation, continued addition of $MgCl_2$ and NaOH then soon leads to a re-increase in the amount of free ions, until critical conditions are again established and a second (or third) event of nucleation takes place. Thereby, the level of supersaturation required for nucleation to occur decreases from step to step, as polymer is progressively consumed upon particle formation (reducing the net inhibitory effect) and heterogeneous nucleation on already existing brucite structures is likely associated with lower barriers. Free ion products determined at the end of this iterative process are very close to those obtained immediately after primary nucleation in the reference experiment (*cf.* Fig. 4c), suggesting that PAA does not affect the nature of the formed phase(s).

Fig. 5 shows a selection of cryo-TEM micrographs taken from samples that were drawn at different stages of the titration assay with added PAA, namely near the first/main maximum of $n_{free}(Mg^{2+})$ (Fig. 5a), after the first drop (Fig. 5b), near the second maximum (Fig. 5c), and after the second drop (Fig. 5d). This sequence of images reveals that $Mg(OH)_2$ nucleation in the presence of poly(acrylic acid) affords very fine platelets, which initially are significantly smaller (<100 nm) and more aggregated than in the reference experiment (Fig. 5a), probably due to particle cross-linking by the organic polymer. Despite their defined shapes, these platelets do not exhibit coherent scattering in ED patterns at the beginning. On the other hand, there was no evidence for the presence of (diffuse) disordered structures (like in Fig. 3d) or any polymer-induced stabilisation of amorphous precursors – in contrast to effects observed for PAA in $CaCO_3$ crystallisation.[40] With time and continued addition of $MgCl_2$ and NaOH (Fig. 5b–d), the platelets undergo a ripening process and grow in size (up to *ca.* 200 nm in diameter), but never reach the dimensions of the individual hexagons in the reference experiment (*cf.* Fig. 3b). In parallel, the total number of particles as well as their density in aggregated structures increases, accompanied by the occurrence of single spots and finally almost continuous rings in corresponding diffraction patterns, which can all be assigned to crystalline brucite.[20,52] Cryo-TEM images

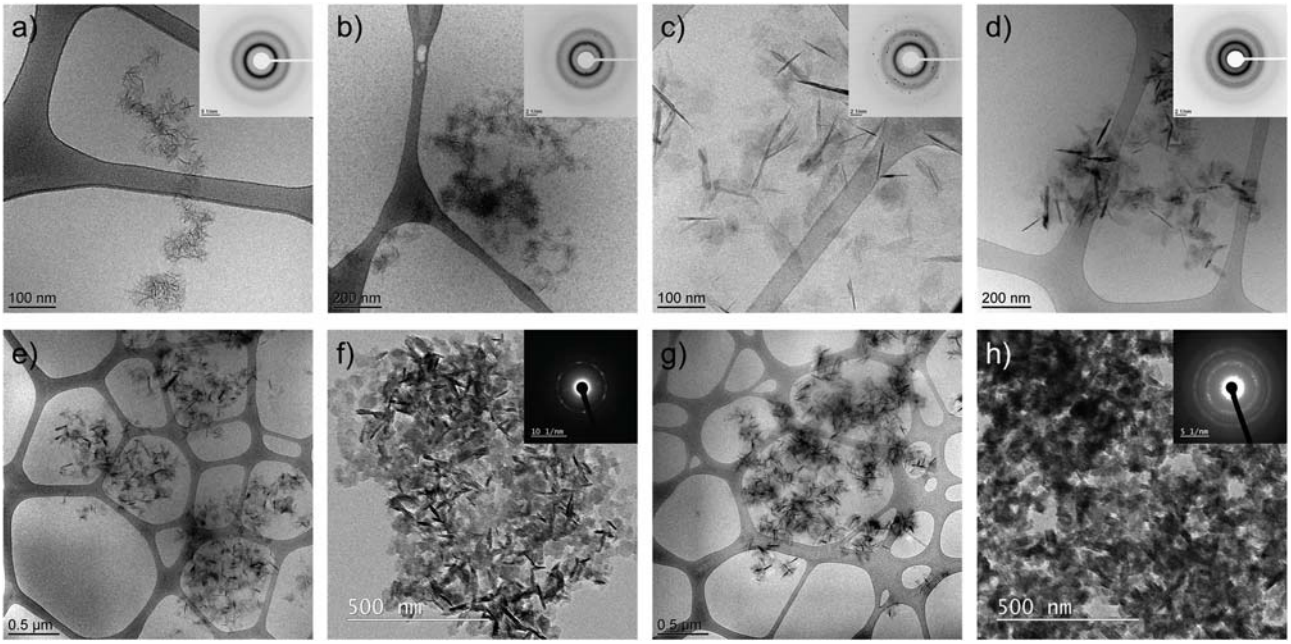

Fig. 5 Characterisation of particles formed during potentiometric titration in the presence of poly(acrylic acid) by means of transmission electron microscopy in (a–e and g) vitrified state under cryogenic conditions and (f and h) dry state at ambient temperature. Samples were drawn near the following characteristic points in the corresponding $n_{free}(Mg^{2+})$ profile (*cf.* Fig. 4a, where the time intervals for sampling are indicated by dashed lines and arrows): (1) first/main maximum (a), (2) first minimum (b, e and f), (3) second maximum (c), and (4) second minimum (d, g and h). The inserted electron diffraction patterns identify the particles as being either amorphous (a) or crystalline with single spots (b and c), arcs (f) or full rings (d and h). All observed reflections can be assigned to crystalline brucite.

acquired at lower magnification for samples drawn near the first (Fig. 5e) and second (Fig. 5g) minimum of $n_{free}(Mg^{2+})$ illustrate that the abundance and size of the aggregated structures increases with time and every new nucleation event, as expected. This notion is further corroborated by TEM analyses performed on the same samples at ambient temperature after drying (Fig. 5f and h), which show dense networks with almost powder-like diffraction patterns.

The role of PAA in $Mg(OH)_2$ crystallisation under the present conditions thus appears to be threefold: first, the polymer inhibits initial phase separation – for reasons that require further studies, although it may be speculated that the transition of chloride-containing magnesium complexes to pure hydroxide-based nucleation precursors is hindered by the polyelectrolyte. Second, PAA has a miniaturising effect on the formed brucite particles, arguably due to the growth-inhibiting influence observed in potentiometric titrations (*cf.* Fig. 4) and the fact that at the time when the system becomes unstable against phase separation, the nominal level of supersaturation is utterly high and many nuclei will thus be formed in a burst-like event. It is also possible that at the time of nucleation, the polycarboxylate carries large amounts of magnesium ions (much like a "sponge") and thus provides local domains enriched in relevant species, where nucleation will preferentially take place – in analogy to the calcium sponges of sulfated (macro)molecules reported to be located around the nucleation sites in the formation of nacre formation.[53] This might explain the absence of more stable/extensive amorphous mineral structures in the polymer-containing system, as ripening towards more ordered states should proceed faster in a microenvironment of locally enhanced supersaturation. Third, the polymer triggers ample aggregation of brucite platelets into extended network-like structures, presumably *via* adsorption on $Mg(OH)_2$ surfaces and bridging of multiple particles (like a "glue"), which should eventually yield a hybrid material of inorganic magnesium hydroxide mineral and organic polymer (note that at the time of the first maximum in Fig. 4a, the molar ratio of Mg^{2+} and monomeric AA units is about 10 : 1, rendering the role of the polymer as "glue" reasonable).

Finally, precipitates present at the end of the titration experiments shown in Fig. 1 (reference) and Fig. 4 (PAA) were isolated by filtration and analysed after drying with respect to structure and composition using X-ray diffraction and IR spectroscopy (Fig. 6). Powder XRD patterns confirm that the formed materials consist of crystalline brucite,[20,52] in line with observations made by electron diffraction (*cf.* Fig. 3 and 5), in both the presence and absence of PAA (Fig. 6a). As all occurring reflections can be assigned to brucite, there is no evidence for any other phases in the data, such as magnesium carbonate or mixed hydroxide–carbonates (which may result from in-diffusion of atmospheric CO_2). Moreover, the peaks in the diffractograms of the PAA-containing material are generally broader than in the reference sample, which is consistent with the smaller primary particle sizes induced by the polymer as observed by TEM (*cf.* Fig. 5). IR

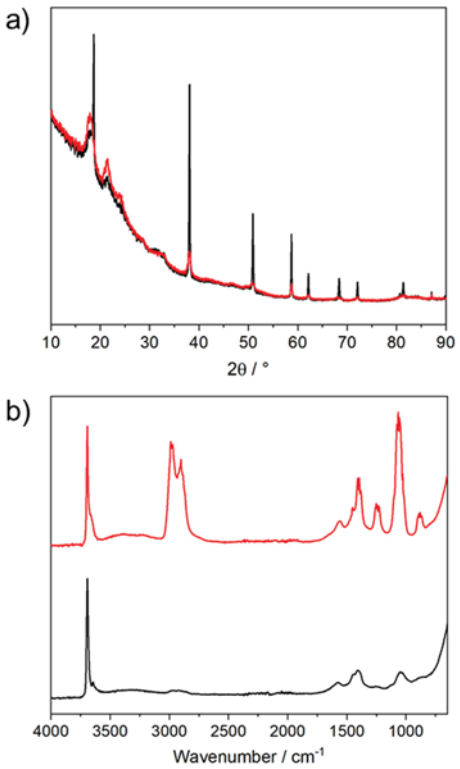

Fig. 6 Characterisation of solid precipitates isolated at the end of potentiometric titration experiments with (red curves) and without (black curves) added poly(acrylic acid) by means of a) powder X-ray diffraction and b) ATR-IR spectroscopy.

spectra of precipitates isolated from the reference experiment without additive (black curve in Fig. 6b) are dominated by the sharp and intense O–H stretching vibration in crystalline brucite at 3698 cm^{-1}.[54] Alongside, a smaller band located at *ca.* 1575 cm^{-1} is observed, which likely originates from bending vibrations of associated water molecules. Furthermore, the split peak at 1450/1410 cm^{-1} and the band at *ca.* 1040 cm^{-1} indicate the presence of certain amounts of amorphous carbonate phases,[55] resulting from apparently inevitable uptake of CO_2 by the alkaline mixtures despite the used protective nitrogen atmosphere. For precipitates formed in the presence of PAA (red curve in Fig. 6b), IR spectroscopy provides clear evidence that the polymer is associated to the inorganic phase in relatively large amounts: next to the O–H stretching vibration of brucite, the spectrum shows several intense bands that are characteristic for the polycarboxylate, such as the aliphatic stretching modes of the acrylic backbone between 3000 and 2800 cm^{-1} as well as multiple other peaks in the range of 1800–600 cm^{-1} caused by C–H deformation and different COOH-related vibrations.[56]

This demonstrates that PAA does not only behave as a potent modifier of the progress of brucite crystallisation from solution, but also becomes an essential part of the formed solid material *via* spontaneous co-precipitation – leading to an organic/inorganic composite whose structure and properties warrant deeper investigations in the future.

Summary & conclusions

In this work, we have established a new titration-based assay that allows the early stages of magnesium hydroxide crystallisation from solution to be monitored in real time and at constant pH. The method uses an ion-selective electrode and a pH sensor to track the free (and bound) amounts of the relevant ions (Mg^{2+} and OH^-) prior to, during and after nucleation. Combined with powerful *ex situ* characterisation by means of (cryogenic) transmission electron microscopy, this approach delivers deep insights into the species and processes involved in $Mg(OH)_2$ nucleation and growth both in the neat mineral system and under the influence of additives.

Specifically, potentiometric titrations performed in the absence of additives showed that, while the general features of the obtained profiles resemble those reported for other minerals like calcium carbonate, ion binding stoichiometries in the pre-nucleation regime are complex in the $Mg(OH)_2$ system and suggest association of Mg^{2+} with both hydroxide and chloride, leading to clusters that may bear net charges. In further analogy with other minerals, a disordered (amorphous) phase is involved in the nucleation of solid magnesium hydroxide, which however exhibits a highly transient character and soon gives way to hexagonal platelets that then grow in size. Addition of poly(acrylic acid) as a typical antiscalant led to a drastic delay of $Mg(OH)_2$ nucleation (as expected), but did not affect ion association equilibria in solution to any noticeable extent. After nucleation, the polymer showed strong interactions with the formed solid phase and inhibited growth, which resulted in a downsizing of primary particles and yielded brucite nanoplatelets that were intimately interspersed with co-precipitated organic polymer. This latter observation appears promising in the context of the synthesis of brucite nanomaterials with controlled sizes for various applications,[15–19] while the spontaneous hybridisation of the inorganic mineral with organic polymer may give rise to additional interesting properties that require further investigations. Apart from that, the methodology developed in the present study is now available for further in-depth analyses of pre- and early post-nucleation phenomena in the $Mg(OH)_2$ system, which may be targeted at conditions that are more relevant to brucite scaling in industrial settings (*e.g.* higher temperatures, different pH values, *etc.*)[24–27] or used to screen potential alternative (*i.e.* more efficient and/or sustainable) chemistries for antiscaling and to understand their mode(s) of action.

Author contributions

Conceptualisation: AK, HC, DG & MK; investigation: JS, JKB, MD, AESVD, HC, DG & MK; methodology: JS, JKB, MD, DG & MK; formal analysis: JS, JKB, MD, AESVD & MK; project administration: AK, HC & MK; supervision: HC, DG & MK; visualisation: JS, JKB, MD, AESVD & MK; writing (original draft): JS, JKB & MK; writing (review & editing): JS, JKB, MD, AK, AESVD, HC, DG & MK.

Conflicts of interest

There are no conflicts to declare.

Acknowledgements

The authors thank Dr. Philipp Müller (BASF SE) for help with the interpretation of some of the TEM data. Parts of this work were funded by BASF SE in the framework of a collaboration with the University of Konstanz.

Notes and references

1 J. J. De Yoreo, P. U. P. A. Gilbert, N. A. J. M. Sommerdijk, R. L. Penn, S. Whitelam, D. Joester, H. Zhang, J. D. Rimer, A. Navrotsky, J. F. Banfield, A. F. Wallace, F. M. Michel, F. C. Meldrum, H. Cölfen and P. M. Dove, *Science*, 2015, **349**, aaa6760.
2 D. Gebauer, M. Kellermeier, J. D. Gale, L. Bergström and H. Cölfen, *Chem. Soc. Rev.*, 2014, **43**, 2348–2371.
3 Y. Y. Kim, A. S. Schenk, J. Ihli, A. N. Kulak, N. B. J. Hetherington, C. C. Tang, W. W. Schmahl, E. Griesshaber, G. Hyett and F. C. Meldrum, *Nat. Commun.*, 2014, **5**, 4341.
4 A. E. S. Van Driessche, T. M. Stawski and M. Kellermeier, *Chem. Geol.*, 2019, **530**, 119274.
5 D. Gebauer, J. D. Gale and H. Cölfen, *Small*, 2022, 2107735.
6 D. Gebauer, A. Völkel and H. Cölfen, *Science*, 2008, **322**, 1819–1822.
7 P. J. M. Smeets, K. R. Cho, R. G. E. Kempen, N. A. J. M. Sommerdijk and J. J. De Yoreo, *Nat. Mater.*, 2015, **14**, 394–399.
8 H. Du and E. Amstad, *Angew. Chem., Int. Ed.*, 2020, **59**, 1798–1816.
9 W. J. E. M. Habraken, J. Tao, L. J. Brylka, H. Friedrich, L. Bertinetti, A. S. Schenk, A. Verch, V. Dmitrovic, P. H. H. Bomans, P. M. Frederik, J. Laven, P. van der Schoot, B. Aichmayer, G. de With, J. J. De Yoreo and N. A. J. M. Sommerdijk, *Nat. Commun.*, 2013, **4**, 1507.
10 C. J. S. Ibsen, D. Chernyshov and H. Birkedal, *Chem. – Eur. J.*, 2016, **22**, 12347–12357.
11 X. Yang, M. Wang, Y. Yang, B. Cui, Z. Xu and X. Yang, *Phys. Chem. Chem. Phys.*, 2019, **21**, 14530–14540.
12 J. Baumgartner, A. Dey, P. H. H. Bomans, C. Le Coadou, P. Fratzl, N. A. J. M. Sommerdijk and D. Faivre, *Nat. Mater.*, 2013, **12**, 310–314.
13 J. Scheck, B. Wu, M. Drechsler, R. Rosenberg, A. E. S. Van Driessche, T. M. Stawski and D. Gebauer, *J. Phys. Chem. Lett.*, 2016, **7**, 3123–3130.
14 G. Zhu, M. L. Sushko, J. S. Loring, B. A. Legg, M. Song, J. A. Soltis, X. Huang, K. M. Rosso and J. J. De Yoreo, *Nature*, 2021, **590**, 416–422.
15 G. J. Simandl, S. Paradis and M. Irvine, *Geosci. Canada*, 2007, **34**, 57–64.
16 Y. Wang, X. Yang, H. Peng, F. Wang, X. Liu, Y. Yang and J. Hao, *ACS Appl. Mater. Interfaces*, 2016, **8**, 9925–9935.

17 G. Balducci, L. Bravo-Diaz and D. H. Gregory, *CrystEngComm*, 2017, **19**, 6067–6084.
18 H. Wang, Z. He and Y. Ni, *J. Wood Chem. Technol.*, 2008, **28**, 55–65.
19 J. Nie and S. Z. Yi, *Adv. Mater. Res.*, 2014, **1073–1076**, 949–954.
20 X. Pan, Y. Wang, Z. Chen, D. Pan, Y. Cheng, Z. Liu, Z. Lin and X. Guan, *ACS Appl. Mater. Interfaces*, 2013, **5**, 1137–1142.
21 T. Santos, A. P. Luz, C. Pagliosa and V. C. Pandolfelli, *J. Am. Ceram. Soc.*, 2016, **99**, 461–469.
22 H. Schuhmacher and L. Schillak, *Bull. Mar. Sci.*, 1994, **55**, 672–679.
23 L. Zhao, L. Sang, J. Chen, J. Ji and H. H. Teng, *Environ. Sci. Technol.*, 2010, **44**, 406–411.
24 A. L. Harrison, I. M. Power and G. M. Dipple, *Environ. Sci. Technol.*, 2013, **47**, 126–134.
25 C. Chieng and G. H. Nancollas, *Desalination*, 1982, **42**, 209–219.
26 A. E. Al-Rawajfeh, H. Glade and J. Ulrich, *Desalination*, 2005, **182**, 209–219.
27 K. Krömer, S. Will, K. Loisel, S. Nied, J. Detering, A. Kempter and H. Glade, *Heat Transfer Eng.*, 2015, **36**, 750–762.
28 A. Alhamzah, E. J. Smith and C. Fellows, *Ind. Eng. Chem. Res.*, 2015, **54**, 2201–2207.
29 D. H. Klein, M. D. Smith and J. A. Driy, *Talanta*, 1967, **14**, 937–940.
30 A. Packter, *Cryst. Res. Technol.*, 1985, **20**, 329–336.
31 X. Song, S. Sun, D. Zhang, J. Wang and J. Yu, *Front. Chem. Sci. Eng.*, 2011, **5**, 416–421.
32 S. K. Myasnikov, A. P. Chipryakova and N. N. Kulov, *Theor. Found. Chem. Eng.*, 2013, **47**, 505–523.
33 T. Santos, A. P. Luz, C. Pagliosa and V. C. Pandolfelli, *J. Am. Ceram. Soc.*, 2015, **99**, 461–469.
34 Q. Yuan, Z. Lu, P. Zhang, X. Luo, X. Ren and T. D. Golden, *Mater. Chem. Phys.*, 2015, **162**, 734–742.
35 L. Lu, Q. Hua, J. Tang, Y. Liu, L. Liu and B. Wang, *Cryst. Res. Technol.*, 2018, **53**, 1700130.
36 J. Hövelmann, C. V. Putnis and L. G. Benning, *Minerals*, 2018, **8**, 346.
37 X. Zhang, A. S. Lea, A. M. Chaka, J. S. Loring, S. T. Mergelsberg, E. Nakouzi, O. Qafoku, J. J. De Yoreo, H. T. Schaef and K. M. Rosso, *Nat. Mater.*, 2022, **21**, 345–351.
38 J. Shin, C. J. Choi, T. H. Kim and J. M. Oh, *Cryst. Growth Des.*, 2018, **18**, 5398–5405.
39 M. Kellermeier, A. Picker, A. Kempter, H. Cölfen and D. Gebauer, *Adv. Mater.*, 2014, **26**, 752–757.
40 P. I. Schodder, M. B. Gindele, A. Ott, M. Rückel, R. Ettl, V. Boyko and M. Kellermeier, *Phys. Chem. Chem. Phys.*, 2022, **24**, 9978–9989.
41 C. Rodriguez-Navarro, A. Burgos-Cara, F. Di Lorenzo, E. Ruiz-Agudo and K. Elert, *Cryst. Growth Des.*, 2020, **20**, 4418–4432.
42 B. Madeja, Phage Display Screening for Cement Systems, *PhD thesis*, University of Konstanz, 2018.
43 D. L. Parkhurst, *User's Guide to PHREEQC: a Computer Program for Speciation, Reaction-Path, Advective-Transport, and Inverse Geochemical Calculations*, U.S. Geological Survey, Lakewood, 1995.
44 D. R. Lide, *CRC Handbook of Chemistry and Physics*, CRC Press, Boca Raton, 2004.
45 X. Cheng, P. L. Varona, M. J. Olszta and L. B. Gower, *J. Cryst. Growth*, 2007, **307**, 395–404.
46 D. Gebauer, H. Cölfen, A. Verch and M. Antonietti, *Adv. Mater.*, 2009, **21**, 435–439.
47 A. Verch, D. Gebauer, M. Antonietti and H. Cölfen, *Phys. Chem. Chem. Phys.*, 2011, **13**, 16811–16820.
48 S. L. P. Wolf, K. Jähme and D. Gebauer, *CrystEngComm*, 2015, **17**, 6857–6862.
49 L. Qi, H. Cölfen, M. Antonietti, M. Li, J. D. Hopwood, A. J. Ashley and S. Mann, *Chem. – Eur. J.*, 2001, **7**, 3526–3532.
50 T. Wang, J. Mitchell, H. Borner, H. Cölfen and M. Antonietti, *Phys. Chem. Chem. Phys.*, 2010, **12**, 11984–11992.
51 J. Scheck, M. Drechsler, X. Ma, M. T. Stöckl, J. Konsek, J. B. Schwaderer, S. M. Stadler, J. J. De Yoreo and D. Gebauer, *J. Chem. Phys.*, 2016, **145**, 2119171–2119178.
52 C. Henrist, J. P. Mathieu, C. Vogels, A. Rulmont and R. Cloots, *J. Cryst. Growth*, 2003, **249**, 321–330.
53 L. Addadi, D. Joester, F. Nudelman and S. Weiner, *Chem. – Eur. J.*, 2006, **12**, 980–987.
54 S. De Angelis, P. Manzari, M. C. De Sanctis, E. Ammannito and T. Di Iorio, *Icarus*, 2016, **280**, 315–327.
55 E. Foran, S. Weiner and M. Fine, *Sci. Rep.*, 2013, **3**, 1700.
56 M. M. Basuni, M. M. El-Bendary, W. A. Hassan and M. Mohammedy, *Res. J. Pharm., Biol. Chem. Sci.*, 2019, **10**, 135–146.